

Article

# A Study of Two Dimensional Tomography Reconstruction of Temperature and Gas Concentration in a Combustion Field Using TDLAS

Pengshuai Sun <sup>1,2</sup> , Zhirong Zhang <sup>1,2,\*</sup>, Zhe Li <sup>1,3</sup>, Qiang Guo <sup>1</sup> and Fengzhong Dong <sup>1,2,3,\*</sup>

<sup>1</sup> Anhui Provincial Key Laboratory of Photonic Devices and Materials, Anhui Institute of Optics and Fine Mechanics, Chinese Academy of Sciences, Hefei 230031, China; sunpengshuai521@126.com (P.S.); lily0317@mail.ustc.edu.cn (Z.L.); qguo@aiofm.ac.cn (Q.G.)

<sup>2</sup> Key Lab of Environmental Optics & Technology, Anhui Institute of Optics and Fine Mechanics, Chinese Academy of Sciences, Hefei 230031, China

<sup>3</sup> School of Environmental Science & Optoelectronic Technology, University of Science and Technology of China, Hefei 230026, China

\* Correspondence: zhangzr@aiofm.ac.cn (Z.Z.); fzdong@aiofm.ac.cn (F.D.); Tel.: +86-0551-6559-5001 (F.D.)

Received: 30 July 2017; Accepted: 20 September 2017; Published: 25 September 2017

**Abstract:** Based on tunable diode laser absorption spectroscopy (TDLAS), two-dimensional (2D) distribution reconstructions of gas concentration and temperature are realized using an algebraic reconstruction technique (ART). The influence of the beam distribution and grid size on combustion field reconstruction is investigated to attain optimal reconstruction results with a limited number of beams. Under limited optical-path numbers, it shows that a better spatial resolution is attainable only when the laser beam paths are vertical and parallel to the symmetry axis of the combustion field. Furthermore, experiments with 16 beam paths using one and two flat flame combustion fields are carried out in different fuel-air equivalence ratios under room temperature. The results are in agreement with the simulation results, and the time resolution is less than 1 s.

**Keywords:** absorption; spectroscopy; diode lasers; temperature; combustion diagnostics; tomographic imaging

## 1. Introduction

In combustion-related systems, measurements of temperature and species concentrations are necessary to fundamentally understand the combustion, optimize the operation process, and improve the combustion efficiency. In recent years, many diagnostic techniques used for measurement of combustion characterization, such as laser light scattering [1,2], molecular filtered Rayleigh scattering (FRS) [3], coherent anti-stokes Raman scattering (CARS) [4], planar laser induced fluorescence (PLIF/LIF) [5–7], have been reported. Although these techniques mentioned above have a number of advantages compared to traditional contact measurement, there are still some inevitable limitations. The FRS and CARS have excellent monitoring capability for high-temperature and extreme conditions, but they cannot provide accurate measurements in low-pressure and low-temperature conditions. Similarly, the PLIF/LIF technique takes advantages of a high spatial resolution and a fast response time, but it has difficulties attaining absolute concentration measurements and precise calibration of free radicals. Moreover, the technology mentioned above suffers from complex optical systems and difficulties associated with expensive equipment.

Tunable diode laser absorption spectroscopy (TDLAS) has been widely used for the detection of various gases and high enthalpy flows [8]. TDLAS usually measures path-averaged information along the laser beam and is thus restricted to flows with near-uniform properties [9]. It was first employed

for the measurement of temperature and species concentration simultaneously in combustion flows by Wang [10]. Line-of-sight tunable diode laser absorption spectroscopy (LOS-TDLAS) sensors for gas temperature and species concentration only retrieve path-averaged information along the laser beam traditionally. Nevertheless, there are still some researchers who applied LOS-TDLAS to diagnose the non-uniformity flow fields based on multiple absorption lines with only one optical beam. For instance, Sanders developed a sensor for oxygen gas temperature distributions [11]. Liu and Zhang studied the temperature and water vapor distributions [12,13]. The multi-spectral LOS-TDLAS technique can retrieve one-dimensional temperature and species distribution, but it is still limited in the application of practical combustion conditions. In recent years, TDLAS is combined with the computed tomography (CT) to form a new measurement method called tunable diode laser absorption tomography (TDLAT). The absorption spectrum effects of spatial variations can also be compensated in fluid properties. It has been developed for measuring 2D distributions of temperature and gas concentration. Many validation tests of the TDLAT have been done on the University of Virginia's Supersonic Combustion Facility and on the NASA Langley Direct-Connect Supersonic Combustion Test Facility [14–17]. For instance, Ma et al. designed a hyperspectral tomography (HT) system that can measure the 2D distribution of temperature and H<sub>2</sub>O concentration simultaneously with a temporal resolution of 50 kHz at 225 spatial grid points [16]. In addition, Xu developed an on-line tomography system that includes two distributed feedback (DFB) laser diodes and fan-beam illumination from five views and 60 rays measurements [18]. In fact, the distributions of temperature and chemical species should be measured in real time and fast response to provide important feedback to the boiler-control, for example, at incinerator facilities and thermal power plants. Therefore, the above detection methods cannot be directly applied to the real-time measurement of dynamic flames systems; the reasons are as follows: (1) the rotating probing beams or target leads to a reduction in temporal responses; (2) the complicated optical and mechanical structures; (3) the powerful computer needed for off-line computation and analysis.

The object of this work is to study an on-line measurement system to monitor the 2D distributions of temperature and H<sub>2</sub>O mole fraction on the dynamic flames using TDLAT. In order to illustrate the influence of beam distribution and grid number on symmetric and asymmetric combustion field reconstruction, the numerical simulations are also introduced as important research content. Moreover, an 8 × 8 reconstruction scheme is designed with a 1395 nm DFB diode laser. Then, the combustion parameters and reconstructed image models under one and two flat flame furnaces are investigated. The measurements demonstrate the ability of TDLAT sensing to monitor temperature and gas concentration distributions in harsh practical environments.

## 2. Absorption Spectroscopy Fundamentals

As mentioned above, TDLAT consists of both TDLAS and CT technology. TDLAS is used to obtain the spectral information in various positions around the measurement space, and the CT technology is then used to reconstruct 2D images of the temperature and gas concentration with above transmission signals. When a laser at frequency  $\nu$  [cm<sup>-1</sup>] enters a gas sample with a path length of  $L$  [cm], the absorbance  $\alpha_\nu$  is expressed as [19]

$$\alpha_\nu = \int_0^L P(x)C(x)S[T(x)]\phi dl \quad (1)$$

where  $x$  is the absorbing species,  $P(x)$  [atm] is the local total pressure,  $C(x)$  is the molar fraction of the absorbing species,  $T(x)$  [K] is the local temperature, and  $\phi$  [cm] is the normalized line shape function. For atmosphere pressure and a high temperature, the line shape is usually approximated by a Voigt profile [20,21]. The line strength of molecular transition  $S$  [T(x)] [cm<sup>-2</sup>atm<sup>-1</sup>] is a function of temperature as follows [22]:

$$S(T) = S(T_0) \frac{Q(T_0)}{Q(T)} \frac{T_0}{T} \exp \left[ -\frac{hcE''_i}{k} \left( \frac{1}{T} - \frac{1}{T_0} \right) \right] \left[ 1 - \exp \left( \frac{-hcv_{0,i}}{kT} \right) \right] \left[ 1 - \exp \left( \frac{-hcv_{0,i}}{kT_0} \right) \right]^{-1} \quad (2)$$

where  $Q(T)$  is the partition function of the absorbing molecule [23],  $T_0$  [K] is the reference temperature,  $k$  [J/K] is the Boltzmann's constant,  $h$  [J·s] is Planck's constant,  $c$  [cm/s] is the speed of light,  $\nu_0$  [ $\text{cm}^{-1}$ ] is the line-center frequency, and  $E''$  [ $\text{cm}^{-1}$ ] is the lower state energy of the transition  $\nu_0$ . Because the line-shape function  $\phi$  is normalized  $\int \phi d\nu \equiv 1$ , the integrated absorbance  $A_\nu$  [ $\text{cm}^{-1}$ ] can be inferred from Equation (1).

$$A_\nu = \int_{-\infty}^{+\infty} \alpha_\nu d\nu = \int_0^L P(x)C(x)S[T(x)]dl \tag{3}$$

The integrated absorbance of two transition lines is measured simultaneously with the same species mole fraction, the same pressure, the same mole fraction, and the same path length. The above two absorbance ratios can be further simplified to the ratio of line strengths  $R$ , which is a function of temperature only as expressed Equation (4) named double-line thermometry [24].

$$R(T) = \frac{A_1}{A_2} = \frac{\alpha_{\nu 1}}{\alpha_{\nu 2}} = \frac{S_1(T)}{S_2(T)} = \frac{S_1(T_0)}{S_2(T_0)} \exp \left[ -\frac{hc}{k} (E_1'' - E_2'') \left( \frac{1}{T} - \frac{1}{T_0} \right) \right] \tag{4}$$

Then, the temperature can be calculated at different temperature dependences:

$$T = \frac{\frac{hc}{k} (E_2'' - E_1'')}{\ln R + \ln \frac{S_2(T_0)}{S_1(T_0)} + \frac{hc}{k} \frac{E_2'' - E_1''}{T_0}} \tag{5}$$

The integrated absorbance areas  $A_\nu$  for each line can be calculated by Voigt line-shape fitting methods. The gas mole fraction can in turn be obtained from the absorption of either transition with the known temperature, pressure, and path-length in Equation (3). However, this double-line thermometry actually obtains a path-averaged value because of the inherent assumption of a uniform temperature distribution along the line of sight. For the 2D distributions of temperature and gas concentration, the test section is divided into  $M \times N$  grids, as shown in Figure 1. Meanwhile, the target gas concentration and temperature are assumed to be uniform in each small grid. The optical path length  $L_{i,j}$  of the  $i$ -th laser beam within the  $j$ -th grid can be calculated according to the two intersecting position of the grid and beam. It should be noted that the numbers of discretized grids, views, and laser beams are important for the accuracy of the tomographic image.

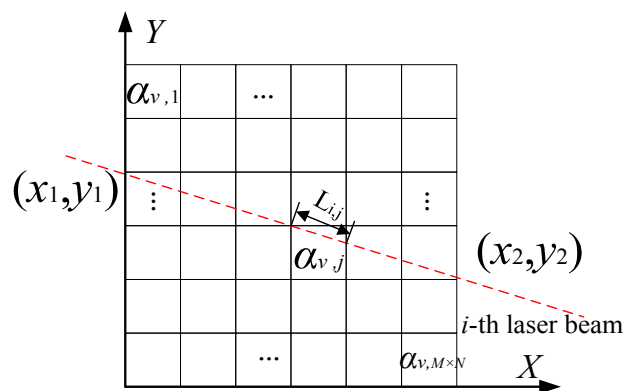


Figure 1. A geometric description of a projection beam and measurement region.

According to Equation (3), the integrated absorbance of the  $i$ -th laser beam  $A_{\nu,i}$  can be expressed as

$$A_{\nu,i} = \sum_j^{M \times N} \alpha_{\nu,j} L_{i,j} = \sum_j^{M \times N} [PS(\nu, T)C]_{\nu,j} \tag{6}$$

$(i = 1, 2 \dots I; j = 1, 2 \dots M \times N)$

where  $\alpha_{v,i}$  is the absorption coefficient in the  $j$ -th grid.  $M \times N$  and  $I$  are the total grid and beams number, respectively. If using two wavelengths with  $I$  laser beams, then Equation (6) can be rewritten in matrix equation as

$$\begin{bmatrix} L_{1,1} & L_{1,2} & \cdots & L_{1,M \times N} \\ L_{2,1} & L_{2,2} & \cdots & L_{2,M \times N} \\ \vdots & \vdots & \vdots & \vdots \\ L_{I,1} & L_{I,2} & \cdots & L_{I,M \times N} \end{bmatrix} \begin{bmatrix} \alpha_1 \\ \alpha_2 \\ \vdots \\ \alpha_{M \times N} \end{bmatrix}_v = \begin{bmatrix} A_1 \\ A_2 \\ \vdots \\ A_I \end{bmatrix}_v \quad (7)$$

The matrix  $L$  can be determined by geometrical arrangement. The integrated absorbance  $A_{v1}$  and  $A_{v2}$  are obtained with measurements. In this work, the absorption coefficients  $\alpha_v$  can be calculated by solving the linear equation, Equation (7). The linear equation is iteratively solved using the algebraic reconstruction technique (ART) [25] as

$$\alpha_j(k+1) = \alpha_j(k) + \lambda \frac{A_i - \sum_{j=1}^{M \times N} \alpha_j(k) L_{i,j}}{\sum_{j=1}^{M \times N} L_{i,j}^2} L_{i,j} \quad (8)$$

$(i = 1, 2, \dots, I; j = 1, 2, \dots, M \times N)$

where  $k$  is the iteration index in the ART procedure, and  $\lambda$  ( $0 < \lambda < 2$ ) is the relaxation coefficient that plays an important role in accuracy performance and determining convergence rate [26]. It is evident that the  $\lambda$  represents the contribution of the absorption at  $j$ -grid to the integral  $i$ -th beam. Therefore, the  $\lambda$  of conventional ART should be replaced by an automatic adjustment relaxation parameter during the reconstruction process, named the modified adaptive algebraic reconstruction technique (MAART) [27]. The  $\lambda$  of Equation (8) is expressed as

$$\lambda = \beta \frac{\alpha_j(k) L_{i,j}}{\sum_{j=1}^{M \times N} \alpha_j(k) L_{i,j}} \quad (9)$$

where  $\beta$  is a constant during the calculation. The  $\beta$  value would be recommended for selection from 0.1 to 0.3, which depends on the number of grids and beams. The reconstruction is terminated when the change of absorption coefficient  $\varepsilon$  in Equation (10) between two consecutive iterations is less than  $1 \times 10^{-6}$ .

$$\alpha_j(k+1) - \alpha_j(k) \leq \varepsilon (\varepsilon = 10^{-6}) \quad (10)$$

The absorbances  $\alpha_{v1,j}$  and  $\alpha_{v2,j}$  in the  $j$ -th grid are obtained by performing the tomographic reconstruction. Finally, the temperature  $T_j$  in  $j$ -th grid can be retrieved from Equations (4) and (5), the H<sub>2</sub>O mole fraction can be calculated from Equation (11).

$$C_j = \frac{\alpha_{v1,j}}{S_1(T_j)} \quad (11)$$

### 3. Numerical Simulation and Analysis

In order to evaluate the efficiency of the MAART and assess the influences of the view angles and numbers, numerical simulations are carried out. Four stationary phantom flames and a square geometry of  $8 \times 8$  grids are considered for simultaneous combustion imaging reconstructions. The different flame temperature imaging  $T^{set}$  and the H<sub>2</sub>O concentration imaging  $C^{set}$  are generated using a Gaussian function and a Random function as shown in Figures 2 and 3, respectively.

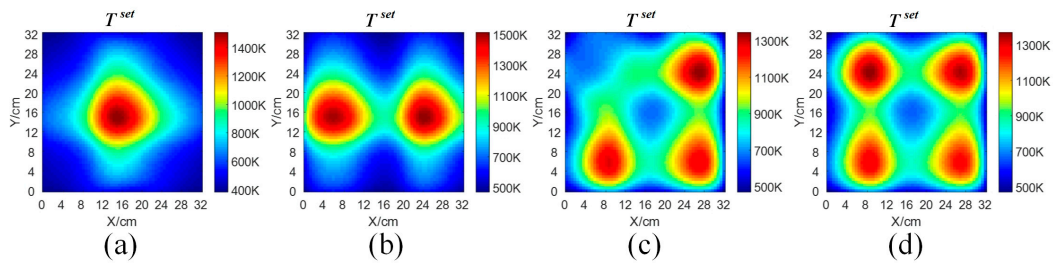


**Figure 2.** Four different distributions of temperature phantoms in the simulation. (a) One flame, (b) Two flames, (c) Three flames, and (d) Four flames.

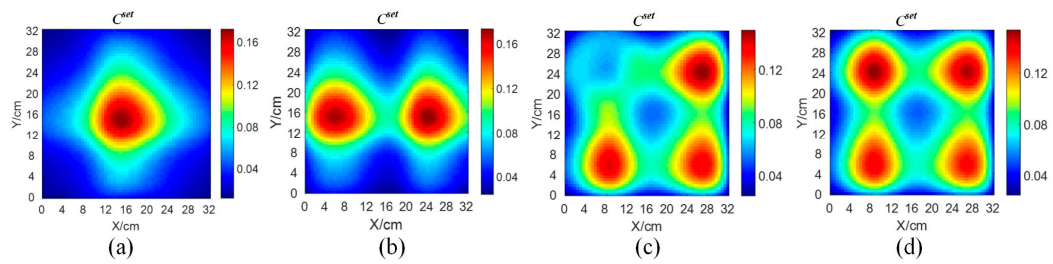


**Figure 3.** Four different distributions of H<sub>2</sub>O concentration in the simulation. (a) One flame, (b) Two flames, (c) Three flames, and (d) Four flames.

Including one flame to four flames, the set temperature distribution  $T^{set}$  are set at  $1500\text{ K} \pm 50\text{ K}$  in the high temperature region and  $400\text{ K} \pm 50\text{ K}$  in the low temperature region. Typically, the H<sub>2</sub>O concentration distribution is generally well correlated with the temperature distribution in a hydrocarbon flame. Therefore, the set volume fractions of H<sub>2</sub>O  $C^{set}$  in the measurement grids are assumed to be  $0.17 \pm 0.005$  and  $0.015 \pm 0.005$ , correspondingly. It is known that the orientation of the view and the number of rays per view has a significant bearing on the quality of reconstruction [28,29]. Therefore, we assumed four different laser beams distributions to study the influence on the reconstruction in simulations. As shown in Figure 4, the number of laser beams included is 16, 18, 32, and 44 with multi-projection. The integrated absorbance is obtained by simulated line-of-sight integration for two water vapor (H<sub>2</sub>O) absorption lines  $7165.82\text{ cm}^{-1}$  and  $7164.91\text{ cm}^{-1}$ . Spectroscopic parameters for the absorption transitions such as line-strengths, lower state energy, coefficients for their temperature dependency, and broadening coefficients are selected from the HITRAN (High Resolution Transmission) 2008 database, as shown in Table 1. Meanwhile, in order to select the most suitable spectral line couples, the numerical simulation is carried out using the above database. The two absorption lines simulations are shown in Figure 5, and the known parameter constants as  $P = 1\text{ atm}$ ,  $L = 32\text{ cm}$ ,  $T = 500\text{ K}$ ,  $C = 0.2\%$ , and  $T = 1500\text{ K}$ ,  $C = 15\%$ . Simulated line-of-sight data are inverted using the MAART, which is introduced in the above theoretical section.

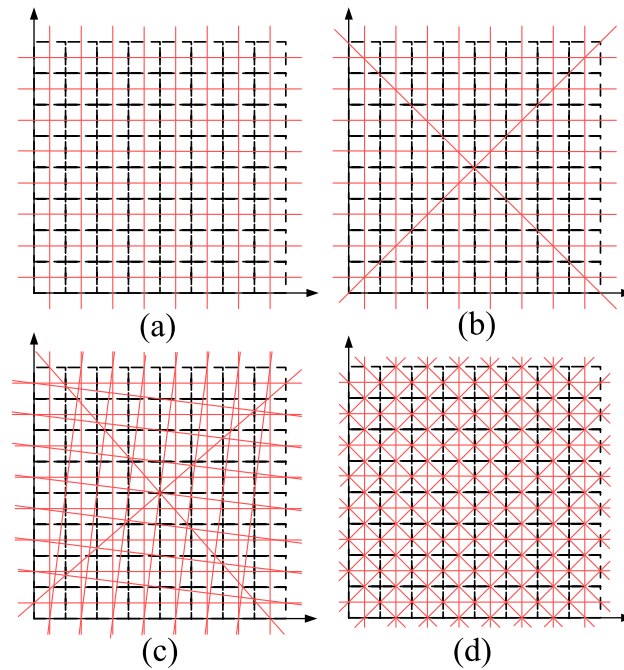


**Figure 4.** Geometric descriptions of the variety laser beams distribution. (a) 16 laser beams, (b) 18 laser beams, (c) 32 laser beams, and (d) 44 laser beams. (Red lines stand for different laser beams).

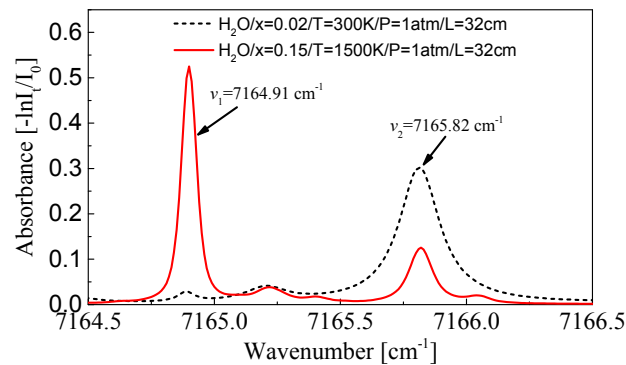


**Figure 5.** The simulated two H<sub>2</sub>O absorption spectra ( $v_1 = 7164.91 \text{ cm}^{-1}$  and  $v_2 = 7165.82 \text{ cm}^{-1}$ ) at  $T = 300 \text{ K}$ ,  $x = 2\%$  (black dot line) and  $1500 \text{ K}$ ,  $x = 15\%$  (red solid line).

Furthermore, the tomographic images have been compared with the four simulated flames, which are discretized into  $M \times N$  grids ( $M = N = 8$ ). The quality of reconstructed results for distributions of both temperature and H<sub>2</sub>O concentration are evaluated by the mean relative error  $e_T$  and  $e_C$  as Equations (11) and (12), respectively.

$$e_T = \sum_i^{M \times N} \left( \left| T_i^{cal} - T_i^{set} \right| / T_i^{set} \right) / (M \times N) \quad (12)$$

$$e_C = \sum_i^{M \times N} \left( \left| C_i^{cal} - C_i^{set} \right| / C_i^{set} \right) / (M \times N) \quad (13)$$

where  $T^{cal}$  and  $C^{cal}$  denote the calculated temperature and the H<sub>2</sub>O concentration of reconstructed distributions. Similarly,  $T^{set}$  and  $C^{set}$  stand for the set temperature and the H<sub>2</sub>O concentration, respectively.

Figure 6 shows the  $e_T$  and  $e_C$  variation curves for different simulation flames under four beam distributions. The value of  $e_T$  and  $e_C$  are reduced with increasing the numbers of views and laser beams. The relative errors of temperatures are less than the concentration reconstruction results. The reason is that the integral area errors caused a greater impact on concentration results from the weak absorption in the peripheral low temperature regions of flame. For the centrosymmetry phantoms of flame as shown in Figure 2a,b,d, we have better reconstruction results when the laser beam paths are vertical and parallel to the symmetry axis of the flame as shown in Figure 4a and the beam number is 16. However, for the non-centrosymmetric phantoms of flame, like in Figures 2c and 3c, we do not have an acceptable and practical reconstruction result when the beam number is 16 and the beam paths are not vertical and parallel to the symmetry axis of the flame. Increasing the number of views and beams,  $e_T$  and  $e_C$  are reduced to less than 0.05 and 0.1, respectively, when the number of beams are 32 and 44, as shown in Figure 4c,d. Therefore, the better spatial resolution could be gained only when the laser beam paths are vertical and parallel to the symmetry axis of the combustion field under the limited number of light paths.

**Table 1.** The selected absorption transition spectral parameters.

Parameter	Wavenumber/cm <sup>-1</sup>	Line Strength /cm <sup>-2</sup> atm <sup>-1</sup> (@300 K)	Lower State Energy/cm <sup>-1</sup>	Line Separation/cm <sup>-1</sup>
$v_1$	7164.91	0.00385	1394	1.09
$v_2$	7165.82	0.14409	212	

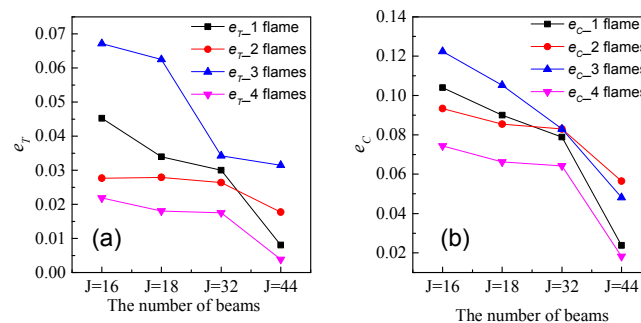


**Figure 6.** (a) The mean relative errors of temperature on the different number of beams. The  $e_{T\_1}$  flame,  $e_{T\_2}$  flames,  $e_{T\_3}$  flames, and  $e_{T\_4}$  flames are the temperature mean relative errors within one, two, three, and four flames. (b) The mean relative errors of H<sub>2</sub>O concentration on the different number of beams. The  $e_{C\_1}$  flame,  $e_{C\_2}$  flames,  $e_{C\_3}$  flames, and  $e_{C\_4}$  flames are the H<sub>2</sub>O concentration mean relative errors within one, two, three, and four flames.

#### 4. Experiment Process and Analysis

The TDLAS-based tomography system is shown in Figure 7a. Figure 7b shows a photograph of the optical test section and the configuration of the probe beams: 8 horizontally and 8 vertically, and with a spacing of 4 cm between neighboring probe beams. To be specific, the diode laser controller and function generator provide stable temperature and precise current controlling signals for a DFB laser. Thus, two vapor transitions  $v_1 = 7165.84 \text{ cm}^{-1}$  and  $v_2 = 7164.91 \text{ cm}^{-1}$  can be covered by the saw tooth scanning current. The output laser is split into 16 channels with a  $1 \times 16$  fiber coupler. Each separated output beam is firstly collimated by a collimator and then guided through the interest region. Finally, the laser beam comprising absorption information is sampled by two arrays that contain 16 equally spaced photodiodes. Each signal is transferred into the Personal Computer to reconstruct the 2D distributions of temperature and H<sub>2</sub>O mole fraction by the on-line manner modified ART. The sampling data of the photodetector output and the data processing are performed using a LabVIEW 2014 (National Instruments, Austin, TX, USA) program.

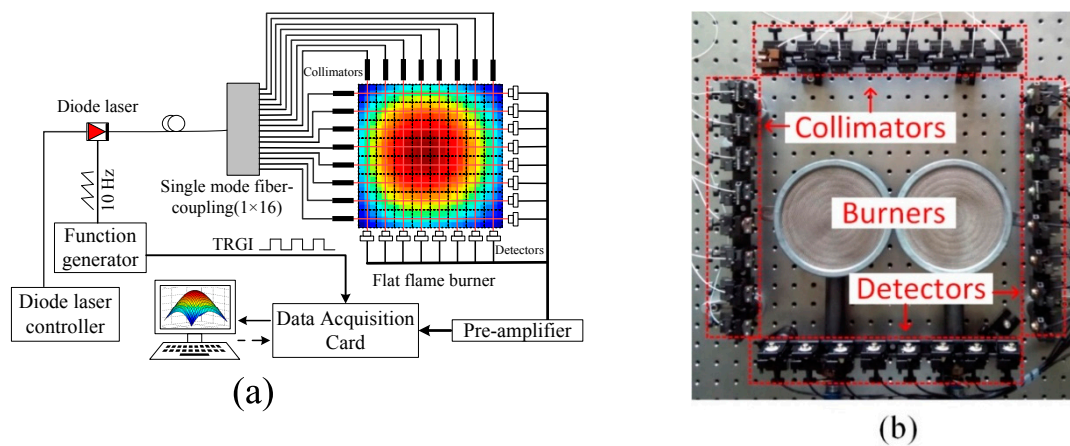


**Figure 7.** The experimental system. (a) The scheme of the tunable diode laser absorption tomography (TDLAT) system with  $8 \times 8$  grids, (b) the photograph of the optical test section: left and upper are 16 collimators, right and under are 16 detectors.

In order to online get the integrated absorbance  $A_v$ , the output wavelength is measured by a wavelength meter 621B-IR (Bristol Instruments, Victor, NY, USA). The output wave number is inversely proportional to the laser drive current, and the variation is  $0.032 \text{ cm}^{-1}/\text{mA}$  obtained by linear fitting. The relationship between the output wavenumber and the laser drive current at different temperatures is shown in Figure 8. In our tomography experiments, the laser temperature is set to  $31 \text{ }^\circ\text{C}$  and the drive current from 63 mA to 118 mA aims to scan over the two vapor absorptions from  $7164.64 \text{ cm}^{-1}$  to  $7166.40 \text{ cm}^{-1}$ . The wavenumber tuning speed of the DFB laser is 10 Hz, and the average of 10 measurements has been done to remove the white noise. A 16-channel synchronous A/D (Analog to Digital) acquisition card is used in this condition, so that the time to record 16 sets of photodetector signal is 1 s including all beam positions. In principle, a more accurate analysis of the integrated absorbance areas at atmospheric pressures can be achieved by fitting the experimental spectra with a Voigt functions, for instance, the standard Humlíček algorithm [30]. It is worth noting that the homogeneous temperature distribution is assumed along the paths of each beam. However, in these experiments, there is no observed improvement in the accuracy of the Voigt fitting, and it will be computationally more intensive than Lorentzian functions. Therefore, the Lorentzian line-shape function is used to fit all the absorption spectrums. Figure 9 shows the final direct absorption signals in flame (red solid line) and in room air (black dot line) for two transitions at  $\nu_1 = 7164.91 \text{ cm}^{-1}$  and  $\nu_2 = 7165.82 \text{ cm}^{-1}$ , respectively. The two integrated absorbance for each channel can be calculated by fitting and the modified ART. In the case of computing efficiency, it takes less than 1 s to reconstruct the images of temperature and  $\text{H}_2\text{O}$  mole fraction. Therefore, the reconstructed 2D distributions of temperature and  $\text{H}_2\text{O}$  mole fraction can be updated and displayed only every 1 s. If we need to analyze the change of combustion more quickly, we need to increase the scanning frequency (hundred or thousand times) to meet the requirements.

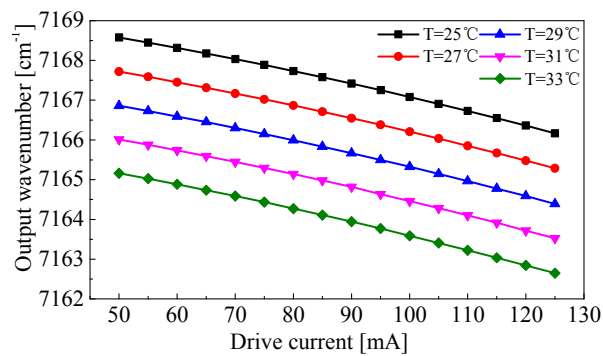


**Figure 8.** The relationship of the output wave number and the laser drive current at different operation temperatures.

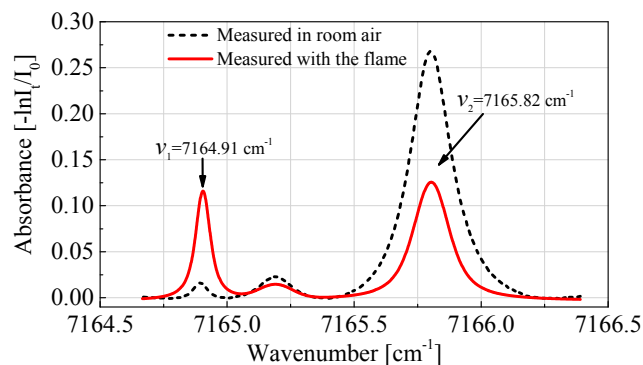


**Figure 9.** The obtained direct absorption signals in room air (black dot line) and in the flame (red solid line) for two transitions at  $\nu_1 = 7164.91 \text{ cm}^{-1}$  and  $\nu_2 = 7165.82 \text{ cm}^{-1}$ , respectively.

In the experiment, a premixed flame is generated by a circular flat flame burner (Holthuis & Associates, Sebastopol, CA, USA). Figure 10 shows the schematic of the burner. The gas fuel and air were mixed in a buffering zone and then passed through the honeycomb grids before flew in to the flame region. In order to build a flat flame, the burner was equipped with a mesh screen. The volumetric flow-rates of the gas fuel and air were accurately controlled by two float-type flowmeters (Shuanghuan, Changzhou, China). The diameter of burner is 12 cm, and the side length of the square measurement region is 32 cm. The height of the laser beams  $8 \times 8$  grids is adjusted 2 cm above the burner surface, as shown in Figure 11. That is to say, the 2D distributions of temperature and  $\text{H}_2\text{O}$  mole fraction on the cross section of the flame at  $H = 2 \text{ cm}$  are reconstructed per second in this experiment. In the combustion process, the air flow rate is set to 20 L/min and three different combustion states are operated by setting the gas fuel ( $\text{CH}_4$ ) flow rates to 1.0 L/min, 1.6 L/min, and 2.1 L/min, which resulted in the fuel–air equivalence ratio ( $\phi$ ) approximate to 0.5, 0.75, and 1, respectively. When the flame is stabilized, the 2D distributions of temperature  $T^{cal}$  and  $\text{H}_2\text{O}$  mole fraction  $C^{cal}$  are obtained. In order to smooth the reconstructed image, the cubic spline interpolating function is applied to the final image data process [31]. In the core of the flame, the value of  $T^{cal}$  and  $C^{cal}$  are larger than beside value in case of a higher equivalent ratio. As shown in Figure 12a, their temperature peaks are 955 K, 992 K, and 1127 K under three different kinds of equivalence ratios, respectively. Based on the analysis, the combustion temperature reaches the highest when the equivalence ratio of the premixed flow is exactly stoichiometric. At the same time, the core flame temperatures have been recorded by a B-type thermocouple, and the measurement results are 905 K, 970 K, and 1066 K, respectively. Therefore, the temperature relative errors between the peaks value of  $T^{cal}$  and the B-type thermocouple (Huakong, Beijing, China) are less than 5.6%. The same effect is observed in the case of the  $\text{H}_2\text{O}$  mole fraction distribution  $C^{cal}$  as in the case of  $T^{cal}$ , as seen in Figure 12b. The core flame theoretical value of  $\text{H}_2\text{O}$

mole fraction is 0.190 when calculated with chemical equilibrium method for a fuel-air equivalence ratio of 1. The H<sub>2</sub>O mole fraction  $C^{cal}$  of the other two combustion states, whose equivalent ratio are 0.75 and 0.5, are 0.146 and 0.099 from theoretical estimates. The experimental measurements are 0.174, 0.135, and 0.092 in the core flame of three combustion states. Therefore, the relative errors between theoretical value and reconstruction  $C^{cal}$  are less than 8.6%. Because the flame region is smaller than the measurement region and the flow disturbance mixes the boundary air into the flame, these cause the H<sub>2</sub>O concentration to be lower than its theoretical value. At the boundary of the flame,  $T^{cal}$  and  $C^{cal}$  gradually decrease to surrounding values because of heat transfer and gas mixing between the combustion products and the surrounding air.

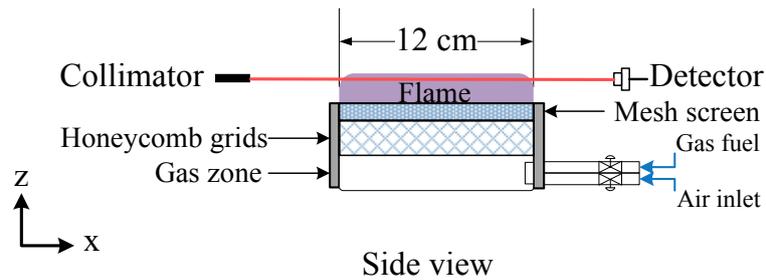


Figure 10. Schematic of the burner.

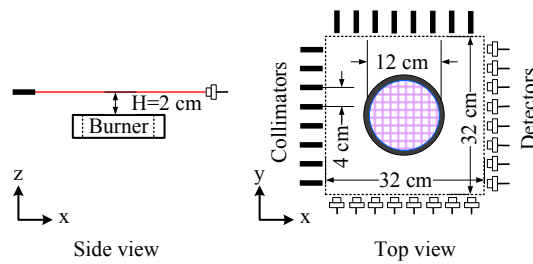


Figure 11. The geometric description of one burner to generate a symmetrical flame shape.

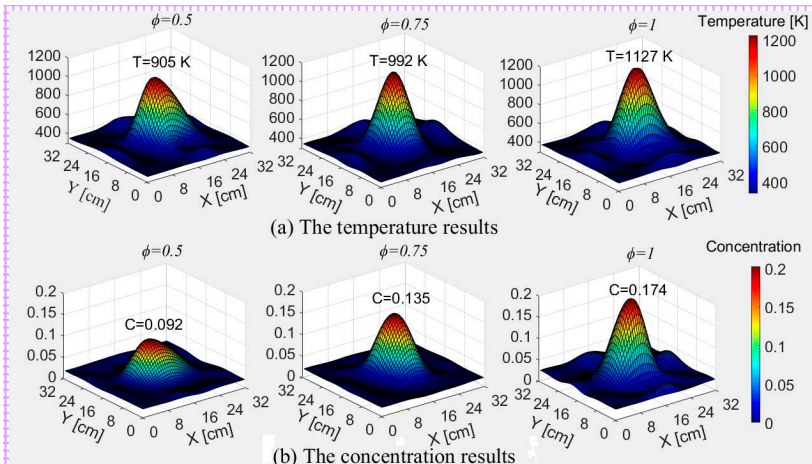
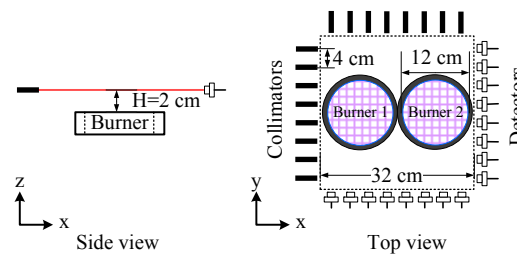


Figure 12. The results of distributions within three kinds of fuel-air equivalence ratio ( $\phi$ ). (a) Temperature distributions and (b) H<sub>2</sub>O concentration distributions.

In order to verify the performance of the tomographic sensor and algorithm, the distributions of temperature and H<sub>2</sub>O mole fraction are reconstructed with two circular flat flames burners as is shown in Figure 13. The divided laser beam grids are also 2 cm high above the two flat flames. In the process of combustion, the air velocity of Burner 1 and Burner 2 are set to 20 L/min and their fuel velocity are

set to 1.8 L/min and 2.0 L/min for different combustion states, respectively. Similarly, the images of 2D distribution of temperature  $T^{cal}$  and H<sub>2</sub>O mole fraction  $C^{cal}$  are shown in Figure 14. The double temperature peaks are 927 K and 996 K at the center of Burner 1 and Burner 2, respectively. Meanwhile, the distribution of  $C^{cal}$  corresponds to the  $T^{cal}$ , and the peak values are 0.094 and 0.134. The  $T^{cal}$  and  $C^{cal}$  out of the combustion area are just above ambient temperature and humidity. The experimental results are well coincident with the theoretical calculation, and yet, the errors are close to 10%. Because the area of effective measurement is larger than the combustion region of interest, the air around the flow has great effects on the results. Although we have obtained good imaging results using the cubic spline interpolating function, the practical image quality is still limited by the finite number of laser beams.



**Figure 13.** The geometric description of two burners to generate a double peaks flame shape.

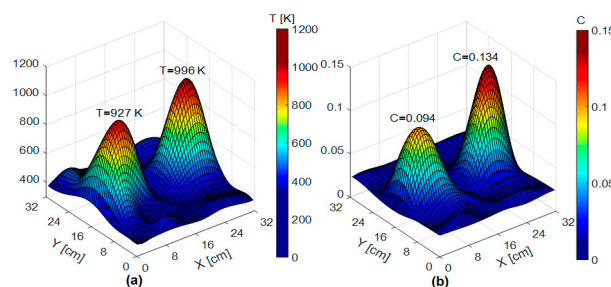


**Figure 14.** Double flat flame burner reconstruction images. (a) Temperature distribution and (b) H<sub>2</sub>O concentration distribution.

## 5. Conclusions

A TDLAT sensor was developed for the simultaneous tomographic imaging of temperature and species concentration. The influences of the number of beams, initial beam angle, and flame distribution on the reconstructed results were analyzed in numerical simulations. Four various flame profiles including symmetrical and asymmetrical distributions were reconstructed using four different beam distributions. The simulation results indicate that the larger numbers of views and laser beams provide a significant contribution in improving the accuracy of the tomographic reconstruction. If working within a limited number of beams, an acceptable error range could still be achieved by keeping the direction of the laser beams vertical and parallel to the symmetry axis. However, this method has some limitations, such as the symmetry of the combustion field needs to be known in advance, and it is impossible to divide into a very dense mesh.

To validate the system performance, the temperature and H<sub>2</sub>O mole fraction distribution of the symmetric premixed flames including one and two burners are reconstructed with an  $8 \times 8$  beam distribution. The distribution images of temperature and H<sub>2</sub>O mole fraction are carried out during three combustion states, and the time resolution is less than 1 s. The results show that the TDLAT sensor is a new effective method for reconstruction of the temperature and H<sub>2</sub>O concentration distribution. Furthermore, it exhibits a good potential for combustion flame monitoring. The dynamic flame shape diagnosis can be used for combustion feedback control in order to maintain combustion efficiency and

minimize pollutant emissions during their operation life cycle. The spatial and temporal resolutions can be increased by improving the scan frequency of DFB laser and data-processing algorithms in the future.

**Acknowledgments:** This work has the support of the National Natural Science Foundation of China (Grant Nos.: 41405034, 41775128, 51504186, 11204320), the External Cooperation Program of Chinese Academy of Sciences (Grant No.: GJHZ1726), the National Key Technology Research and Development Program of the Ministry of Science and Technology of China (Grant No.: 2014BAC17B03), and the Special Fund for Basic Research on Scientific Instruments of the Chinese Academy of Science (Grant No.: YZ201315).

**Author Contributions:** P.S., Z.Z., and F.D. conceived and designed the experiments; P.S. performed the experiments; P.S. and Z.L. analyzed the data; Z.Z. and Q.G. contributed materials; P.S. wrote the paper.

**Conflicts of Interest:** The authors declare no conflict of interest.

## References

1. Laurendeau, N.M. Temperature measurements by light-scattering methods. *Prog. Energy Combust. Sci.* **1988**, *14*, 147–170. [[CrossRef](#)]
2. Fuest, F.; Barlow, R.S.; Chen, J.-Y.; Dreizler, A. Raman/rayleigh scattering and CO-LIF measurements in laminar and turbulent jet flames of dimethyl ether. *Combust. Flame* **2012**, *159*, 2533–2562. [[CrossRef](#)]
3. Kearney, S.P.; Beresh, S.J.; Grasser, T.W.; Schefer, R.W.; Schrader, P.E.; Farrow, R.L. A filtered rayleigh scattering apparatus for gas-phase and combustion temperature imaging. *AIAA J.* **2003**, *41*, 584. [[CrossRef](#)]
4. Vestin, F.; Afzelius, M.; Berger, H.; Chaussard, F.; Saint-Loup, R.; Bengtsson, P.E. Rotational cars thermometry at high temperature (1800 k) and high pressure (0.1–1.55 mpa). *J. Raman Spectrosc.* **2007**, *38*, 963–968. [[CrossRef](#)]
5. Schulz, C.; Sick, V. Tracer-lif diagnostics: Quantitative measurement of fuel concentration, temperature and fuel/air ratio in practical combustion systems. *Prog. Energy Combust. Sci.* **2005**, *31*, 75–121. [[CrossRef](#)]
6. Sick, V.; Drake, M.C.; Fansler, T.D. High-speed imaging for direct-injection gasoline engine research and development. *Exp. Fluids* **2010**, *49*, 937–947. [[CrossRef](#)]
7. Wang, M.; Wang, G.; Qu, D. The laser measurement technology of combustion flow field. In Proceedings of the International Symposium on Photonics and Optoelectronics (SOPO 2014), Suzhou, China, 22–24 August 2014.
8. Bolshov, M.; Kuritsyn, Y.A.; Romanovskii, Y.V. Tunable diode laser spectroscopy as a technique for combustion diagnostics. *Spectrochim. Acta Part B* **2015**, *106*, 45–66. [[CrossRef](#)]
9. Ouyang, X.; Varghese, P.L. Line-of-sight absorption measurements of high temperature gases with thermal and concentration boundary layers. *Appl. Opt.* **1989**, *28*, 3979–3984. [[CrossRef](#)] [[PubMed](#)]
10. Wang, J.Y. Laser absorption methods for simultaneous determination of temperature and species concentrations through a cross section of a radiating flow. *Appl. Opt.* **1976**, *15*, 768–773. [[CrossRef](#)] [[PubMed](#)]
11. Sanders, S.T.; Wang, J.; Jeffries, J.B.; Hanson, R.K. Diode-laser absorption sensor for line-of-sight gas temperature distributions. *Appl. Opt.* **2001**, *40*, 4404–4415. [[CrossRef](#)] [[PubMed](#)]
12. Liu, X.; Jeffries, J.B.; Hanson, R.K. Measurement of non-uniform temperature distributions using line-of-sight absorption spectroscopy. *AIAA J.* **2007**, *45*, 411–419. [[CrossRef](#)]
13. Zhang, G.; Liu, J.; Xu, Z.; He, Y.; Kan, R. Characterization of temperature non-uniformity over a premixed CH<sub>4</sub>-air flame based on line-of-sight TDLAS. *Appl. Phys. B* **2016**, *122*, 9. [[CrossRef](#)]
14. Busa, K.M.; Bryner, E.; McDaniel, J.C.; Goyne, C.P.; Smith, C.T.; Diskin, G.S. Demonstration of capability of water flux measurement in a scramjet combustor using tunable diode laser absorption tomography and stereoscopic PIV. In Proceedings of the 49th AIAA Aerospace Sciences Meeting Including the New Horizons Forum and Aerospace Exposition, Orlando, FL, USA, 4–7 January 2011; pp. 1–14.
15. Busa, K.M.; Ellison, E.N.; McGovern, B.J.; McDaniel, J.C.; Diskin, G.S.; DePiro, M.J.; Capriotti, D.P.; Gaffney, R.L. Measurements on NASA Langley durable combustor rig by TDLAT: Preliminary results. In Proceedings of the 51st AIAA Aerospace Sciences Meeting Including New Horizons Forum and Aerospace Exposition, Grapevine, TX, USA, 7–10 January 2013; AIAA-2013-0696.

16. Ma, L.; Li, X.; Sanders, S.T.; Caswell, A.W.; Roy, S.; Plemmons, D.H.; Gord, J.R. 50-Khz-rate 2D imaging of temperature and H<sub>2</sub>O concentration at the exhaust plane of a J85 engine using hyperspectral tomography. *Opt. Express* **2013**, *21*, 1152–1162. [[CrossRef](#)] [[PubMed](#)]
17. Busa, K.M.; Rice, B.E.; McDaniel, J.C.; Goyne, C.P.; Rockwell, R.D.; Fulton, J.A.; Edwards, J.R.; Diskin, G.S. Direct measurement of combustion efficiency of a dual-mode scramjet via TDLAS and SPIV. In Proceedings of the 53rd AIAA Aerospace Sciences Meeting, Kissimmee, FL, USA, 5–9 January 2015.
18. Xu, L.; Liu, C.; Jing, W.; Cao, Z.; Xue, X.; Lin, Y. Tunable diode laser absorption spectroscopy-based tomography system for on-line monitoring of two-dimensional distributions of temperature and H<sub>2</sub>O mole fraction. *Rev. Sci. Instrum.* **2016**, *87*, 013101–013113. [[CrossRef](#)] [[PubMed](#)]
19. Witzel, O.; Klein, A.; Meffert, C.; Wagner, S.; Kaiser, S.; Schulz, C.; Ebert, V. VCSEL-based, high-speed, in situ TDLAS for in-cylinder water vapor measurements in IC engines. *Opt. Express* **2013**, *21*, 19951–19965. [[CrossRef](#)] [[PubMed](#)]
20. Bolshov, M.A.; Kuritsyn, Y.A.; Liger, V.V.; Mironenko, V.R.; Leonov, S.B.; Yarantsev, D.A. Measurements of the temperature and water vapor concentration in a hot zone by tunable diode laser absorption spectrometry. *Appl. Phys. B* **2010**, *100*, 397–407. [[CrossRef](#)]
21. Sane, A.; Satija, A.; Lucht, R.P.; Gore, J.P. Simultaneous CO concentration and temperature measurements using tunable diode laser absorption spectroscopy near 2.3  $\mu\text{m}$ . *Appl. Phys. B* **2014**, *117*, 7–18. [[CrossRef](#)]
22. Webber, M.E. Diode Laser Measurements of NH<sub>3</sub> and CO<sub>2</sub> for Combustion and Bioreactor Applications. Ph.D. Thesis, Stanford University, Stanford, CA, USA, January 2001.
23. Gamache, R.R.; Kennedy, S.; Hawkins, R.; Rothman, L.S. Total internal partition sums for molecules in the terrestrial atmosphere. *J. Mol. Struct.* **2000**, *517*, 407–425. [[CrossRef](#)]
24. Liu, X.; Jeffries, J.B.; Hanson, R.K.; Hinckley, K.M.; Woodmansee, M.A. Development of a tunable diode laser sensor for measurements of gas turbine exhaust temperature. *Appl. Phys. B* **2005**, *82*, 469–478. [[CrossRef](#)]
25. Wang, F.; Cen, K.F.; Li, N.; Jeffries, J.B.; Huang, Q.X.; Yan, J.H.; Chi, Y. Two-dimensional tomography for gas concentration and temperature distributions based on tunable diode laser absorption spectroscopy. *Meas. Sci. Technol.* **2010**, *21*, 045301. [[CrossRef](#)]
26. Herman, G.T.; Lent, A.; Lutz, P.H. Relaxation methods for image reconstruction. *Commun. ACM* **1978**, *21*, 152–158. [[CrossRef](#)]
27. Li, N.; Weng, C. Modified adaptive algebraic tomographic reconstruction of gas distribution from incomplete projection by a two-wavelength absorption scheme. *Chin. Opt. Lett.* **2011**, *9*, 061201.
28. Wright, P.; Garcia-Stewart, C.A.; Carey, S.J.; Hindle, F.P.; Pegrum, S.H.; Colbourne, S.M.; Turner, P.J.; Hurr, W.J.; Litt, T.J.; Murray, S.C.; et al. Toward in-cylinder absorption tomography in a production engine. *Appl. Opt.* **2005**, *44*, 6578. [[CrossRef](#)] [[PubMed](#)]
29. Guha, A.; Schoegl, I. In Limited view tomography of combustion zones using tunable diode laser absorption spectroscopy: Simulation of an algebraic reconstruction technique. In Proceedings of the ASME 2012 International Mechanical Engineering Congress and Exposition, Houston, TX, USA, 9–15 November 2012.
30. Humlíček, J. Optimized computation of the voigt and complex probability functions. *J. Quant. Spectrosc. Radiat. Transf.* **1982**, *27*, 437–444. [[CrossRef](#)]
31. Kasyutich, V.L.; Martin, P.A. Towards a two-dimensional concentration and temperature laser absorption tomography sensor system. *Appl. Phys. B* **2011**, *102*, 149–162. [[CrossRef](#)]

